MTLA 39 (2025) 102361

Contents lists available at ScienceDirect

Materialia

journal homepage: www.elsevier.com/locate/mtla

Statically recrystallized grain size as a function of prior stored energy level in the A-286 Fe-based superalloy

A. Potenciano [a,*], A. Nicolay [a], A. Da Fonseca Alvarenga [a], O. Danylova [b], J. Dairon [b], M. Bernacki [a], B. Flipon [a], N. Bozzolo [a,c]

[a] Mines Paris, PSL University, Centre for material forming (CEMEF), UMR CNRS, 06904 Sophia Antipolis, France
[b] Aperam Alloys, 58160 Imphy, France
[c] Safran Tech, 78772 Magny Les Hameaux, France

ARTICLE INFO

Keywords:
Static recrystallization
Indentation
Nucleation
Dislocation density
Grain growth
Ebsd

ABSTRACT

A-286 alloy is a Fe-based superalloy used in various engines and gas turbine components. During manufacturing, this alloy is submitted to a solution heat treatment that provides good formability for the subsequent deformation steps. Hence, a good control of grain size evolution is required to avoid the formation of a broad grain size distribution or the growth of abnormally large grains. In this work, a well-controlled strain gradient has been generated by means of indentation tests at room temperature. A specific strain level, calculated by finite element simulations, and the associated dislocation density estimated by the EBSD technique, lead to the activation of selective grain growth during heat treatment after a given incubation time. This study on cold-deformed A-286 alloy allowed a quantitative assessment of recrystallized grain size dependence on stored energy and the identification of the critical stored energy value for grain nucleation, providing a better understanding of A-286 static recrystallization behavior.

1. Introduction

The demanding requirements for high-temperature materials in terms of mechanical properties are constantly increasing. The critical conditions of application to which they are subjected restrain the use of common alloys. As a consequence, superalloys have emerged as the best solution for high-performance applications in extreme conditions, since they can safely maintain optimal mechanical properties at high temperature relative to their melting point [1,2]. For structural application of polycrystalline grades, fine and homogeneous microstructures are most often required in order to optimize the in-service performance and durability of mechanical components [3–5]. In addition, good microstructural and in turn mechanical properties stability must be guaranteed over increasingly long periods of time.

Fe-based superalloys are cost-effective alternatives to the widely used Ni-based superalloy grades in many high-temperature applications, operating in a domain of less extreme temperatures, typically up to ~700 °C. In this context, the A-286 alloy is an Fe-based superalloy employed in the manufacture of engine and gas turbine components for a wide range of sectors, including aeronautics, automotive, hydrogen power generation, and oil & gas [6,7]. For those applications, the A-286 alloy is strengthened by fine and ordered precipitates of coherent face-centered cubic γ'- $Ni_3(Ti, Al)$ phase in the austenitic matrix during aging [8,9]. During the manufacturing process before the ageing treatment, it is submitted to a solution heat treatment at either 980 °C for 1 hour or 900 °C for 2 h that provides good formability for the following deformation steps [10].

Broad and even bimodal grain size distributions or the appearance of coarse grains, up to 100 times larger than the average grain size causing a severe degradation of mechanical properties, have been reported in similar materials annealed after cold or hot deformation [5–7,11–18] as a result of a static recrystallization (SRX) mechanism under critical conditions for which the nucleation density is very low. In the literature, different mechanisms leading to grain boundary migration and grain size evolution have been proposed [11–18]. To date, different terms have been used to describe the emergence of overgrown grains in a

* Corresponding author.
E-mail addresses: antonio.potenciano_carpintero@minesparis.psl.eu (A. Potenciano), alexis.nicolay@minesparis.psl.eu (A. Nicolay), artur.alvarenga@minesparis.psl.eu (A. Da Fonseca Alvarenga), olena.danylova@aperam.com (O. Danylova), jonathan.dairon@aperam.com (J. Dairon), marc.bernacki@minesparis.psl.eu (M. Bernacki), baptiste.flipon@minesparis.psl.eu (B. Flipon), nathalie.bozzolo@safrangroup.com (N. Bozzolo).

https://doi.org/10.1016/j.mtla.2025.102361
Received 2 August 2024; Accepted 3 February 2025
Available online 4 February 2025

microstructure. The term abnormal grain growth (AGG) was formerly indistinctly used to report various cases of selective grain growth. However, this term is only appropriate when the mechanism governing this growth is solely driven by the reduction of the total area of grain boundaries. In this case, some isolated crystals would locally present favorable conditions to grow by capillarity effect, while the overall microstructural evolution is hindered by other metallurgical factors such as second-phase particles, solute segregations, or the presence of a very strong crystallographic texture [11–13,19].

To be differentiated from the former cases, critical grain growth (CGG) will be used for cases where the local and selective growth of some grains is driven by the consumption of prior stored strain energy (SSE). Ni-based superalloys have been observed to be sensitive to CGG, which appears to be the originating mechanism for grain size heterogeneity after annealing [11–16]. The prior level of SSE present in the microstructure before the start of the solution heat treatment has a predominant influence on the subsequent emergence of abnormally large grains (ALGs). Many authors have demonstrated that low-strained microstructures are particularly vulnerable to this CGG occurrence [11–14].

For the CGG occurrence, the prior SSE level can be achieved by either cold or hot deformation, and for each of these cases it is possible to distinguish some differences with respect to the main metallurgical mechanisms:

(1) **If the solution treatment is performed after cold deformation,** the SSE level in the microstructure before heat treatment can be directly linked to the equivalent strain level, since dynamic recrystallization and recovery process are inhibited during cold work. If the SSE level is near to the critical amount of stored energy required to onset the nucleation of new recrystallized grains, the latter will be sparse and able to grow to large extent. In this case, the CGG mechanism results from static recrystallization with low local nuclei density, and is characterized by an incubation time for the development of coarse grains, the incubation time being required to nucleate the few new grains. Increasing strain or SSE level leads to higher nucleation density and smaller and homogeneous recrystallized grains which grow until impinging each other. After recrystallized grains impinge on each other, their growth does not completely stop but is drastically slowed down since it is no longer driven by SSE consumption but only by grain boundary area reduction, which provides a driving pressure that is typically one to two orders of magnitude lower than that associated to SSE. This is the reason why statically recrystallized grain size is primarily controlled by nucleation density.

(2) **If the solution treatment is preceded by hot deformation,** ALGs could arise from nuclei formed during the static recrystallization stage as described in case (1), but also from dynamically recrystallized grains with low stored energy levels, formed during hot working. The strain rate, strain level and temperature of hot deformation, as the regulatory parameters of the resulting SSE levels, could control the occurrence of CGG during subsequent annealing. An incubation time can not be estimated since nucleation can occur before the final solution treatment.

The reported phenomena of selective grain growth in the A-286 alloy appears to be strongly related to the thermomechanical history of the material. The occurrence of CGG in cold-deformed A-286 Fe-based superalloy is investigated in this work. This article proposes an in-depth analysis of the influence of SSE on grain size evolution during high-temperature annealing. The experimental procedure consists in performing indentation tests at room temperature in order to introduce a well-controlled strain gradient in the specimens. After deformation, this initial strained zone was accurately characterized by numerical and experimental methods, and then annealed under different time-temperature conditions in order to allow microstructural evolutions. The same experiments have recently been used to study CGG mechanism in a Ni-based alloy [13]. In this case, the analysis was performed for all samples by associating the morphology and location of the resulting coarse grains with the prior strain levels present before heat treatment. Other microstructural features which may have a direct impact on grain boundary migration, such as the presence of second phase particles, will also be a subject of discussion in the current article.

The aim of this work is to perform a quantitative assessment of recrystallized grain size dependence on stored energy, and of the critical stored energy value for grain nucleation during heat treatment after a given incubation time, which is a requirement in view of setting up a predictive model of the static recrystallization behavior of the alloy.

Various phenomenological models, such as the Avrami relationship [20–22], have been proposed during the past century to model and understand how materials recrystallize during hot deformation. In the last decades, finer approaches, referred to as full field numerical frameworks, were developed, providing an explicit representation of the microstructure allowing an accurate tracking of its evolutions. In contrast with mean field models, full field models consider the topology of grains and the interactions between neighboring grains, so they allow the modeling of local selective grain growth mechanisms such as CGG [23–26]. In some of these frameworks, dynamic recrystallization is modeled through the assessment of strain hardening, recovery and associated dislocation density evolution by phenomenological laws (as described in Section 3.4). Hence, they have the limitation of requiring the thermomechanical history of the sample, which must have undergone a campaign of hot deformation tests, to model SRX. Therefore, this experiment not only provides information regarding the CGG mechanism in the A-286 alloy, but also constitutes an economic and easy-to-reproduce methodology for the perspective of calibrating a static recrystallization phenomenological law.

2. Experimental procedure

2.1. Material

The A-286 superalloy, whose chemical composition is given in Table I, was received in the form of a 10 mm diameter cold drawn bar. Cylindrical specimens (⌀10 mm x 5 mm in length) were initially sectioned from this bar. These samples were first annealed at 1050 °C for 20 min and then water quenched to reach a fully recrystallized reference microstructure. At this stage, an average grain size of 57 μm was evaluated as an equivalent circle diameter (ECD) and few intergranular titanium carbides and nitrides were identified (Fig. 1c). A quite homogeneous initial microstructure can be observed, with the largest grains having an ECD close to 300 μm (Fig. 1b).

2.2. Indentation tests and metallographic preparation

One face of each cylindrical specimen was then prepared by grinding and conventional polishing in order to obtain an adequate surface for indentation (Fig. 2). Indentation tests were conducted using the Wolpert Dia 2Rc hardness machine model, with a spherical Brinell tungsten carbide indenter of 1.56 mm diameter. The applied load was set at 150 kg, which produced an average indentation diameter of 1061 μm with a standard deviation of 6 μm. The total duration of each test was 66 ss, and the loading time was estimated at 40 ss. From this point forward, the indented microstructure will be referred to as the *initial microstructure* or *deformed-state*.

After indentation at room temperature, the specimens were submitted to different heat treatments at 980 °C, 1000 °C or 1025 °C. The samples were introduced into a preheated Carbolite 1200 furnace at one of these three temperatures, held for different times from 10 min to 3.5 h and finally water quenched. In the following, the samples will be identified by their heat treatment parameters (temperature/duration).

Table 1
A-286 superalloy chemical composition.

Element	Fe	Ni	Cr	Ti	Mo	V	Mn	Si	Al	C	S	B
% weight	Base	27.00 – 24.00	16.00 – 13.50	2.35 – 1.90	1.50 – 1.00	0.50 – 0.10	< 2	< 1.0	< 0.35	< 0.08	< 0.03	0.01 – 0.001

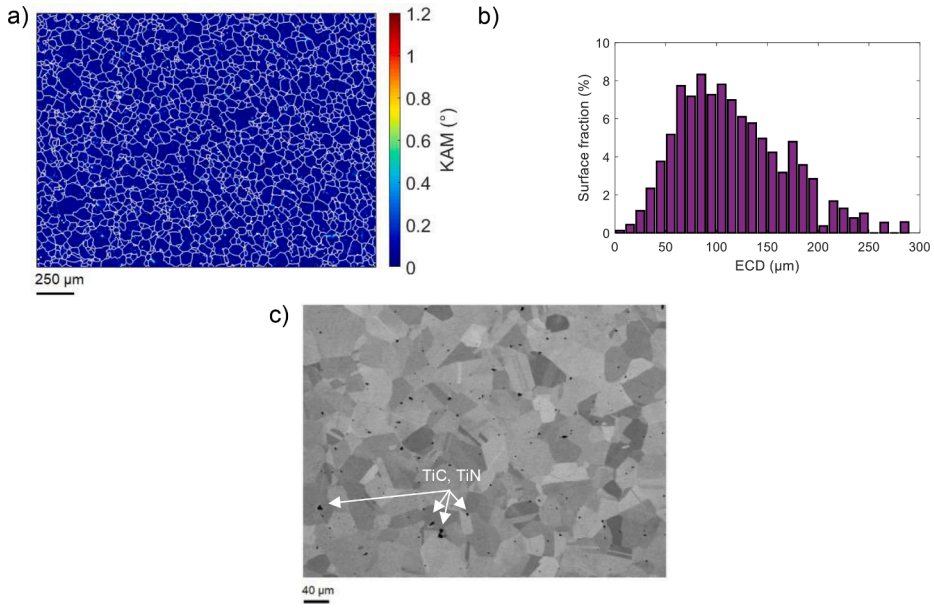

Fig. 1. Initial microstructure in the section plane in the state prior to indentation. a) 2nd order Kernel Average Misorientation (KAM) map with grain boundaries in white (defined by a misorientation angle higher than 10°). b) Grain size surface fraction histogram. c) Backscattered electrons (BSE) image, with TiN or TiC as the black second phase particles that can be found across the microstructure.

After heat treatment, all samples were cut along the axial direction for the purpose of analyzing the microstructure evolution just below the indented zone. The microstructure is analyzed in the transverse section, in the section plane as indicated in Fig. 2. The distance between the observed plane after polishing and the plane that crosses right in the middle of the indentation mark, referred as $\Delta center$, was monitored. $\Delta center$ is estimated directly from the measurement of the indentation diameter and the chord observed on the section plane presented in Fig. 2, carefully carried out after each polishing stage.

The transverse section plane (Fig. 2b) was grinded with SiC abrasive papers, then polished with 3 µm diamond suspension and finally with SiO_2 colloidal suspension, with an average diameter of silica particles of 20 nm. The prepared specimens were analyzed using a Carl Zeiss Supra 40 field emission gun scanning electron microscope (FEGSEM). Microstructural observations were carried out around the indented zone with a Backscattered Electron (BSE) detector. Some specimens have been selected for further Electron Backscatter Diffraction (EBSD) analysis, using a Bruker EBSD $e^{-Flash^{HR}}$ detector controlled by the software package Esprit 2.1, mounted on a Zeiss Supra40 FEG SEM operated at 20 kV, with a 15 mm working distance. The indexing algorithm used allowed acquiring EBSD maps with very few mis-indexed and non-indexed points. The final precision of the measured crystallographic orientation is estimated to be around 0.5° [27]. The step size was selected considering the dimensions of the scanned area and microstructure characteristic sizes, between 0.7 µm to 1.2 µm per pixel. The indexation hit rate was higher than 99 %. The open-source MTEX toolbox version 5.1.1 was used for the post-processing of EBSD data [28], using Matlab R2018a version. The grains must be composed of more than 3 pixels, with a lower threshold of 10 ° misorientation angle to define the grain boundaries. The twins are identified by a 60 ° misorientation along the axis ⟨111⟩ with a tolerance of 5 °. All EBSD data were filtered using the half-quadratic filter developed by Bergmann et al. [29] to reduce measurement noise. The half-quadratic filter effectively removes spatially independent noise from orientation measurement data while maintaining sharp gradients at the grain boundaries and subgrain boundaries [30]. Scanning electron micrographs were obtained using the backscattered electron detector with a 15 kV voltage at a working distance of 10 mm. Orientation data are represented by the Kernel Average Misorientation (KAM) parameter. The KAM parameter is a value assigned to each pixel/point in the EBSD map that indicates the average misorientation angle between that pixel and its neighbors. It can be expressed mathematically by the following formula:

$$KAM(p_i) = \frac{1}{\nu_i} \sum_{j=1}^{\nu_i} \theta_{i,j}, \tag{1}$$

where $\theta_{i,j}$ is the misorientation angle between pixel p_i and pixel p_j, and ν_i is the number of neighboring pixels of p_i. For the calculation of KAM, only first neighbors (1st order KAM) and first and second order neighbors (2nd order KAM) will be considered in this work, and misorientations above 10 °, that correspond to grain boundaries, are ignored.

2.3. Finite element simulation

To describe the equivalent strain field generated by the indentation, a finite element model (FEM) was developed using ABAQUS/Standard commercial simulation software [31]. A 3D model of the cylindrical sample and the spherical indenter has been created, in such a way that several planes that cut the specimen can be generated (which are parallel to the plane of force application) considering $\Delta center$ for each experimental case. The model is controlled by the indenter displacement and the mesh has been adapted in order to ensure a fine description of the strained area. A hexahedral swept fine mesh with elements of type C3D8R has been used, with a mesh size that gradually increases with

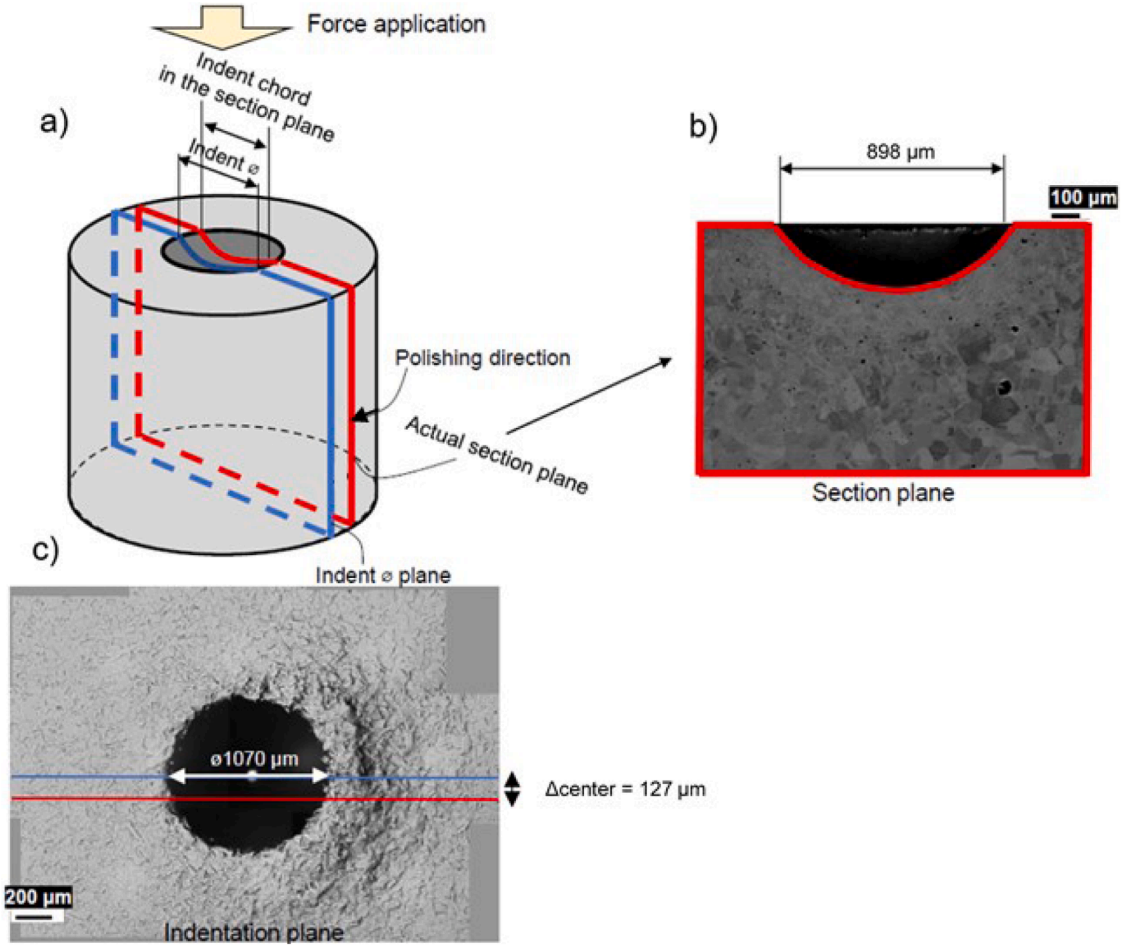

Fig. 2. (a) Schematic representation of the metallographic preparation method (top view). (b) Section plane. (c) Indentation plane before sectioning with the associated *Δcenter* value obtained after polishing.

increasing distance from the indentation area. Additionally, the elastic-plastic behavior considered in the model has been obtained from previous mechanical tests performed at room temperature. A final discharge step has been considered in order to take into account the elastic springback. The friction between the indenter and the specimen has been implemented using a Coulomb friction model with a friction coefficient of $\mu = 0.15$. The equivalent strain field obtained from the finite element analysis is described in Fig. 3.

3. Results and discussion

3.1. Strain field and microstructure characterization

The equivalent strain field can be described by semi-elliptical regions of similar area, each of them associated to a specific range of equivalent plastic strain (PEEQ) values, as shown in Fig. 3. The maximum equivalent strain level ($\varepsilon_{eq} \sim 0.6$) can be found in the region immediately adjacent to the indentation mark, where the friction forces have the greatest impact, as it can be found in Fig. 4c, where the equivalent plastic strain field is represented with a higher number of discretely colored intervals. Then, it gradually decreases with increasing distance

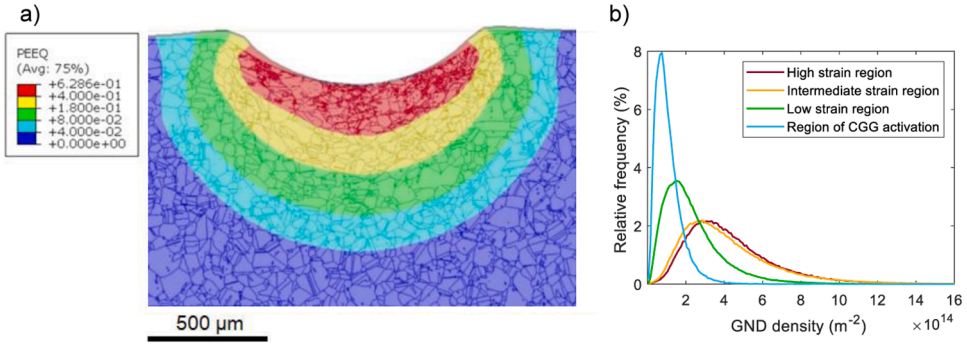

Fig. 3. (a) Equivalent strain field induced by spherical indentation overlapping a grain and twin boundary EBSD map of the deformed state microstructure in the section plane (Δcenter = 144 µm). (b) Relative frequency curves of the GND density in each of the four regions identified by their range of strain values.

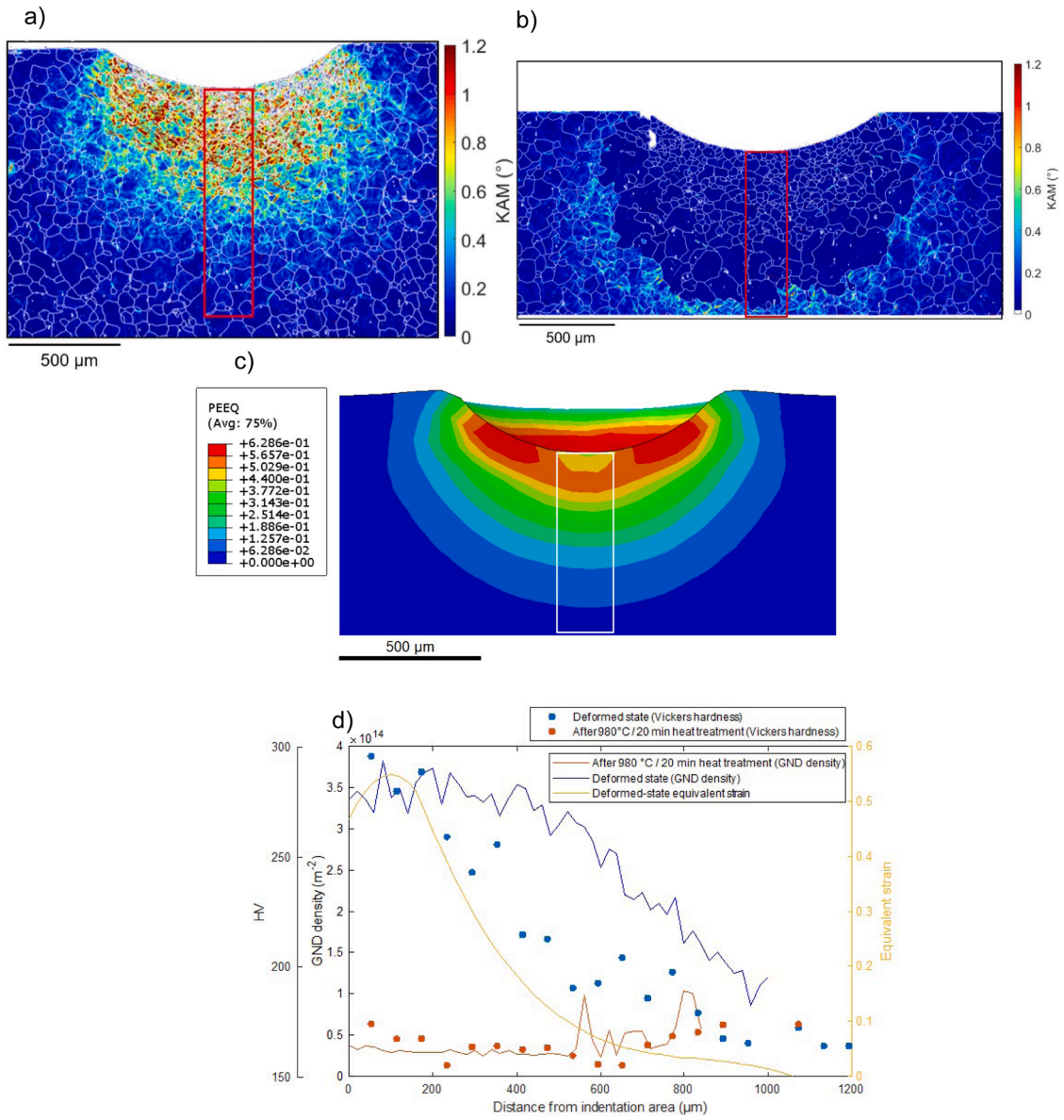

Fig. 4. (a) KAM map of the deformed state. (b) KAM map of the microstructure after a 980 °C/20 min heat treatment. In white, high angle grain boundaries (HAGB). (c) Equivalent plastic strain field of the indented specimen (**Δ**center = 144 μm). (d) GND density (solid blue and orange lines), equivalent strain (solid yellow line) and Vickers micro-hardness profiles (blue and orange points). In blue, deformed state. In orange, after a 980 °C / 20 min heat treatment. The equivalent plastic strain profile and GND density profiles are obtained by averaging x-axis data enclosed within the 200 μm-wide red -or white- rectangle lines in (a), (b) and (c).

to the indented surface (in the central region, the aforementioned decrease in strain begins at a distance of about 170 μm beneath the indentation surface, as indicated in Figs. 4 and Fig. 4d). The shape of the indented area (deduced from the EBSD map of the deformed-state microstructure in the plane section, Fig. 4a) is not perfectly identical to the result of the FE simulation, indicating that friction could be better modelled. The model also shows that the strained area reaches a maximum depth of 700 μm from the indented surface. Four different semi-elliptical regions are defined in Fig. 3, and the density of geometrically necessary dislocations (GNDs) in each of these regions is calculated. The criterion to determine that a grain belongs to a semi-elliptical region is that more than half of their area must be covered by the aforementioned semi-elliptical region. Then, all the grains fulfilling this criterion are selected and the estimation of the density of geometrically necessary dislocations (ρ_{GND}) is carried out by means of the calculation of Nye's dislocation density tensor [32]. From 2D EBSD data, three components of the Nye tensor are calculated, while the other two components can also be estimated. The four remaining components that are not experimentally accessible can then be estimated by minimizing the overall dislocation density [33]. In the GND density frequency graph (Fig. 3b), these four semi-elliptical regions are referred as "high strain", "intermediate strain", "low strain" and "region of CGG activation", as the distance to the indentation area increases and hence GND density gradually decreases.

EBSD analysis were performed on an indented sample in the deformed-state before the solution heat treatment (Fig. 4a), at Δcenter = 144 μm; and after a heat treatment at 980 °C for 20 `min` (Fig. 4b), at Δcenter = 233 μm. In Fig. 4a, the maximum intragranular misorientations are observed in the regions close to the indented zone. Then, intragranular misorientation levels gradually decrease with increasing distance to indentation surface. The map dimensions are 1500 μm x 1900 μm, so the regions subjected to strain are captured on this map, as predicted by the FE model (Fig. 3). In Fig. 4a and b, ρ_{GND} is averaged per horizontal line (x-axis) across the region enclosed by the red box.

In the ρ_{GND} profile of the deformed state (blue curve in Fig. 4d), a

significant decrease of dislocation density with the distance to the indentation area can be observed, which is consistent with the KAM map in Fig. 4a. Remarkably lower ρ_{GND} values are found after a 980 °C/20 min heat treatment (blue curve) due to static recrystallization. It can be observed, however, an increase in ρ_{GND} at a distance of 550 μm from the indentation area, which corresponds to the beginning of the small grains region below the coarse grains band in Fig. 4b. Therefore, according to ρ_{GND} values, two regions can be differentiated in the annealed microstructure: a region of recrystallized grains near the indentation area up to the coarse grains band, and below a region of non-recrystallized grains which might have only undergone recovery, since their ρ_{GND} values are higher than those of the recrystallized grains above, while they are lower than the values that can be found at the equivalent zone in the deformed-state.

This same specimen was submitted to micro-hardness measurements performed with a BUEHLER - Micromet 5124 from the center of the indentation area across the plane section towards the bottom of the sample. A Vickers micro-indenter with a load of 25 g has been used, with a small distance (in the range from 50 to 250 μm) between two consecutive measurements, respecting the criteria of spacing the indentation marks at least 3 times the lateral dimension of the indent [34,35]. The resulting hardness profiles are described in Fig. 4d. In these figures, the dots in orange correspond to the measurements performed in the transverse section plane of the 980 °C/20 min heat-treated state. In blue, the measurements performed in the transverse section plane of the deformed-state. In the deformed-state, high hardness levels, up to 280 HV, can be observed in the vicinity of the indentation area (starting point). Then the values gradually decrease with increasing distance until they reach approximately a value of 200 HV at 500 μm below the starting point. Both profile curves reached the same level of ~160 HV at distances greater than 900 μm from the indentation area. The deformed-state hardness measurements agree well with the equivalent strain field provided by the FE model, although the initial strain increase within 100 μm of the indentation zone has not been captured in the deformed-state hardness curve due to the accuracy limitations of the hardness measurements. In the heat-treated state, as the distance from the indentation mark increases, the hardness levels decrease progressively, associated to the increase in recrystallized grain size, until reaching a plateau slightly above 150 HV, which corresponds to the hardness value of the fully recrystallized reference state, before indentation. Then, at distances beyond 600 μm from the indentation zone, the profile exhibits a hardness increase with a maximum value close to 180 HV, which corresponds to the non-recrystallized zone below the band of coarse grains, as it can be seen in Fig. 4(b). Finally, far from the strained zone, the hardness values slowly decrease to a value around 160 HV.

3.2. Static recrystallization process

Several indented samples were annealed at 980 °C, 1000 °C and 1025 °C for different durations. The microstructures of all the heat-treated indented samples were observed by SEM backscattered electrons (BSE) imaging or analyzed by EBSD. The corresponding data are shown in Fig. 5.

The KAM maps in Fig. 5 demonstrate the formation of two regions during annealing: a non-recrystallized zone and a recrystallized zone in the vicinity of the indentation area as discussed in Fig. 4. All heat-treated

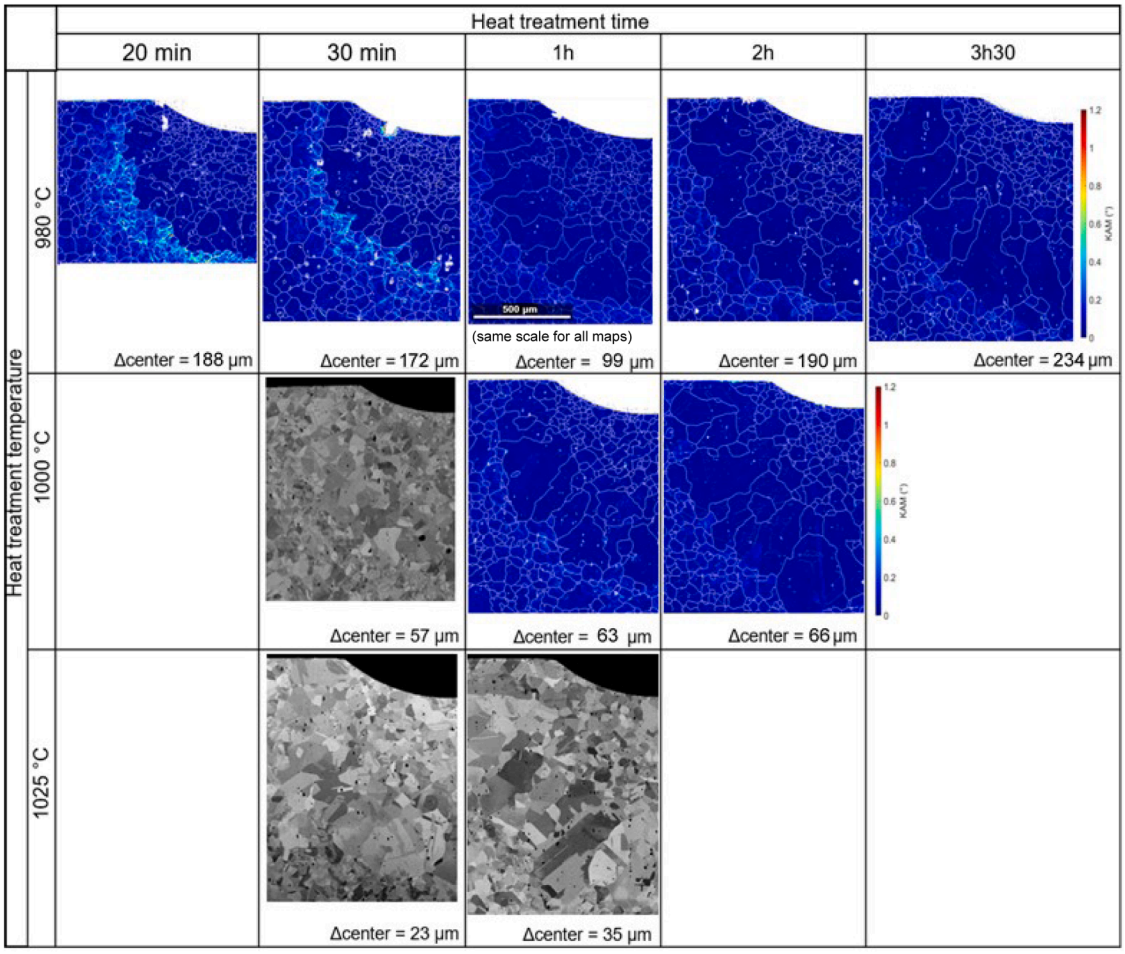

Fig. 5. SEM-BSE images and first order KAM maps of indented samples after heat treatments at 980 °C, 1000 °C and 1025 °C for different durations.

samples present a region of small, equiaxed recrystallized grains in the area adjacent to the indentation mark. Under this area, grain size progressively increases with increasing distance to the indented zone. This gradual increase in grain size is observed until the appearance of a semi-circular band in which the recrystallized grains reach their maximum size. This band of elongated grains expands as the annealing time, or temperature, increases. In all three cases, another region of small grains can be observed below the coarse grains band, with internal BSE contrasts or higher levels of intragranular misorientation, which suggests the presence of residual strain, indicating that the grains below the aforementioned band are non-recrystallized. Therefore, the SSE levels in this non-recrystallized region are not large enough to generate the necessary driving pressure to activate the nucleation process or to be consumed by the adjacent coarse grains which grow within the applied annealing time.

The microstructures shown in the micrographs of Fig. 5 are in good accordance with the equivalent strain field of the FE model (Fig. 3), with coarse grains appearing in low strained zones (where the equivalent plastic strain is near 0.04), and grain size decreasing as the stored energy increases approaching the indentation mark. This is consistent with the mechanism of static recrystallization, since the high levels of SSE close to the indentation zone can promote higher density of new recrystallized nuclei, the growth of which is limited by mutual impingement. Conversely, as the distance to the indentation zone increases, the level of prior SSE gradually decreases, so the active nucleation sites become statistically sparser, allowing recrystallized grains to grow larger for longer times, as can be seen in Fig. 5.

To summarize, the initial strain distribution leads to a non-homogeneous nucleation density during annealing, so the heterogeneous emergence of some new nuclei and their subsequent growth causes the formation of the grain size gradients that can be observed in the Fig. 5. Therefore, recrystallized grain size is a consequence of the density of nuclei (except for the size of the coarse grains band). It can also be seen that the coarse grains have developed an elongated shape, up to 400 μm. This characteristic morphology demonstrates that their growth occurs towards the region of small non-recrystallized grains located below, reducing and hence consuming the remaining stored energy, causing the expansion of the CGG-driven band.

The influence of SSE on the CGG mechanism can be seen in Fig. 6, where the size and localization of the CGG-driven band is defined by its associated strain level at the deformed-state (at the positions of "start" and "end" of the CGG-driven grains band, measured in the heat-treated state). These "start" and "end" positions correspond to the closest and furthest point to the indented area, respectively, from the central region of the CGG band, by only considering the section of the CGG band within the 200 μm wide box illustrated in Figs. 4b and c, for the sake of simplicity.

As shown in Fig. 4d (yellow curve), any distance can be correlated to a deformed-state plastic equivalent strain using the FE model. Therefore, the plastic equivalent strains (in the deformed-state) of the aforementioned points from the upper and lower boundaries of the CGG band are obtained via the results of the FE simulation of the indentation test in those specific points. Not only the distance to the indentation area, but also Δcenter, are considered when identifying the aforementioned upper and lower points of the CGG band and their associated deformed-state PEEQ values in the FE model. Fig. 6 indicates that the CGG mechanism is was active during all heat treatments performed, showing that the CGG-driven grains originate from the furthermost nuclei (i. e. the furthest nuclei from the indentation area) that appear in deformed-state low-strained zones. Moreover, with increasing heat treatment temperature, the CGG-driven grains nucleate in regions with a lower deformed-state PEEQ level, as illustrated in Fig. 6. In the presence of a strain gradient, the fact that a small strain level of less than $\varepsilon < 0.1$ can give place to a nucleus that develops into a CGG-driven grain under the annealing conditions investigated in this work would indicate that a minor strain originated from industrial product manipulation at room temperature poses a severe risk of CGG activation in a subsequent heat treatment process.

In addition to the heat treatments which yield the microstructures shown in Fig. 5, shorter heat treatments were carried out in this work to investigate the time required to trigger the appearance of the coarse grains band. Figs. 7a and b show the microstructure of specimens after heat treatment at 980 °C/10 min and 980 °C/20 min, respectively. The boundaries between recrystallized and non-recrystallized grains are highlighted in yellow. In Fig. 7b, after 20 min of heat treatment at 980 °C, several recrystallized grains can be found entirely below the lower boundary of the recrystallization front from Fig. 7a (which belongs to the microstructure submitted to a 980 °C/10 min heat treatment). These recrystallized grains are hence found further from the indentation area, in a region less-strained (moreover, at a higher Δcenter) than the recrystallization front from the microstructure heat-treated at 980 °C/10 min. As the distance from the indentation area increases and hence dislocation density decreases, incubation time increases. However, the microstructures in Fig. 7 do not provide accurate enough evidence to

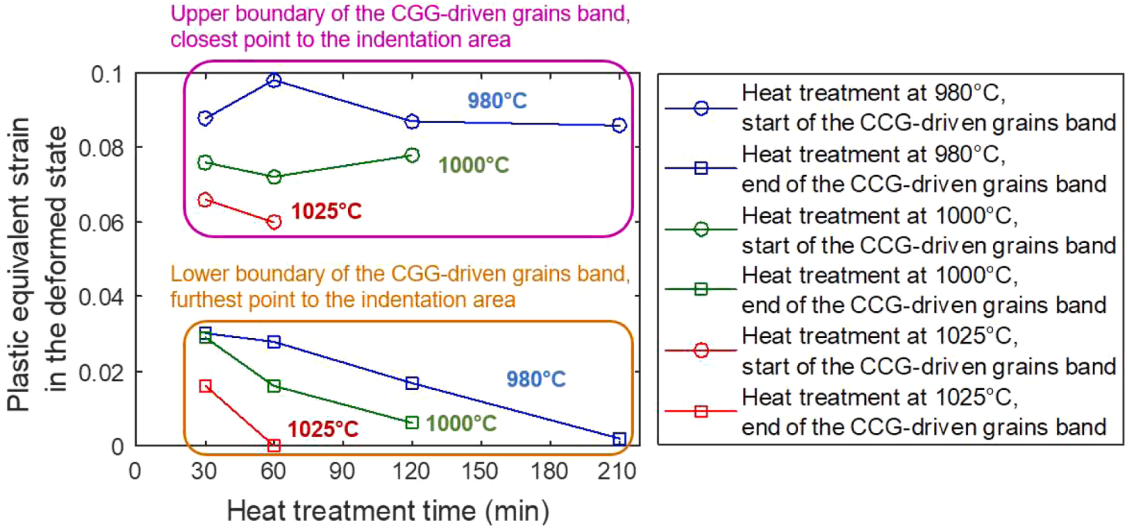

Fig. 6. Deformed-state strain level (before heat treatment) at the boundaries of the CGG-driven grains band (after heat treatment) for different heat treatment time and temperature. To simplify the association between the deformed-state strain level (profile in Fig. 4 d) and the position of the CGG-driven grains band, the measurements are only made within the width of the region enclosed by the red rectangles in Fig. 4 a and b.

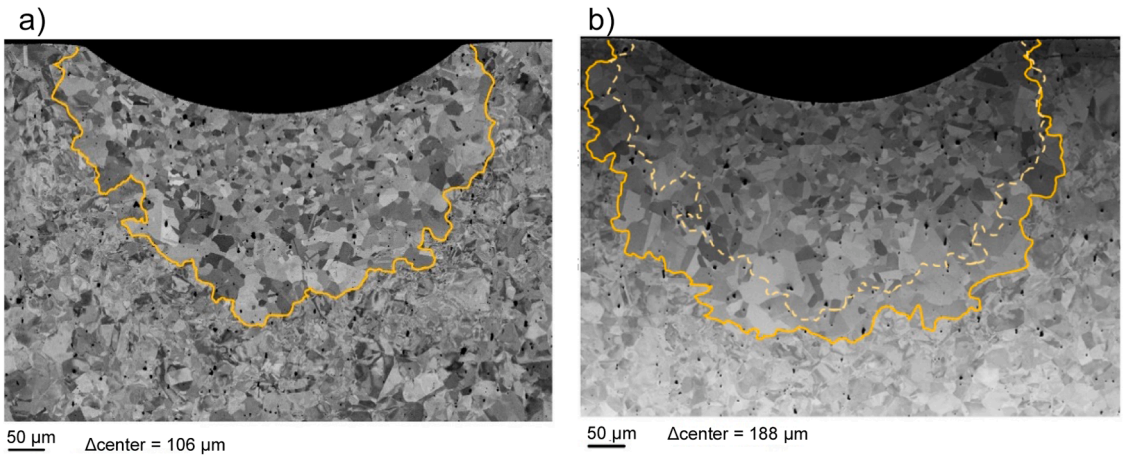

Fig. 7. BSE micrographs of CGG-free specimens after a heat treatment of (a) 980 °C/10 min and (b) 980 °C/20min. Grain boundaries between recrystallized and non-recrystallized grains are indicated in yellow. The recrystallized front from (a) is shown in dashed lines in (b).

determine that there is an active nucleation mechanism (of the nuclei that will give place to the "last" recrystallized grains, the CGG-driven grains) between 10 and 20 min of heat treatment at 980 °C. The CGG mechanism is not extensively triggered between 10 and 20 min of heat treatment at 980 °C, as indicated by the equiaxed morphology of the majority of the recrystallized grains located the furthest from the indentation area, and the aforementioned identification of recrystallized grains (in the 980 °C/20 min heat-treated microstructure) located entirely below the 980 °C/10 min recrystallization front depicted by the dashed profile in Fig. 7b. The recrystallized grain size gradient and thus the longer size of the furthermost grains, i. e. the grains from the recrystallization front, would only be a consequence of the (low) density of nuclei in that region, which decreases with increasing distance to the indentation area.

3.3. *Influence of CGG mechanism on static microstructural evolutions*

During the annealing process, after a given time necessary to trigger the CGG mechanism, the outermost recrystallized grains (i.e. the recrystallized grains adjacent to non-recrystallized regions) will grow towards the non-recrystallized zone as a consequence of the differences in stored energy, as illustrated in Fig. 5. In contrast, the rest of the recrystallized grains will not grow under increasing annealing time or temperature: equiaxial grain growth will early be interrupted by mutual impingement of recrystallized grains, and hence, recrystallized grain size will be inversely related to the density of nuclei near the indented

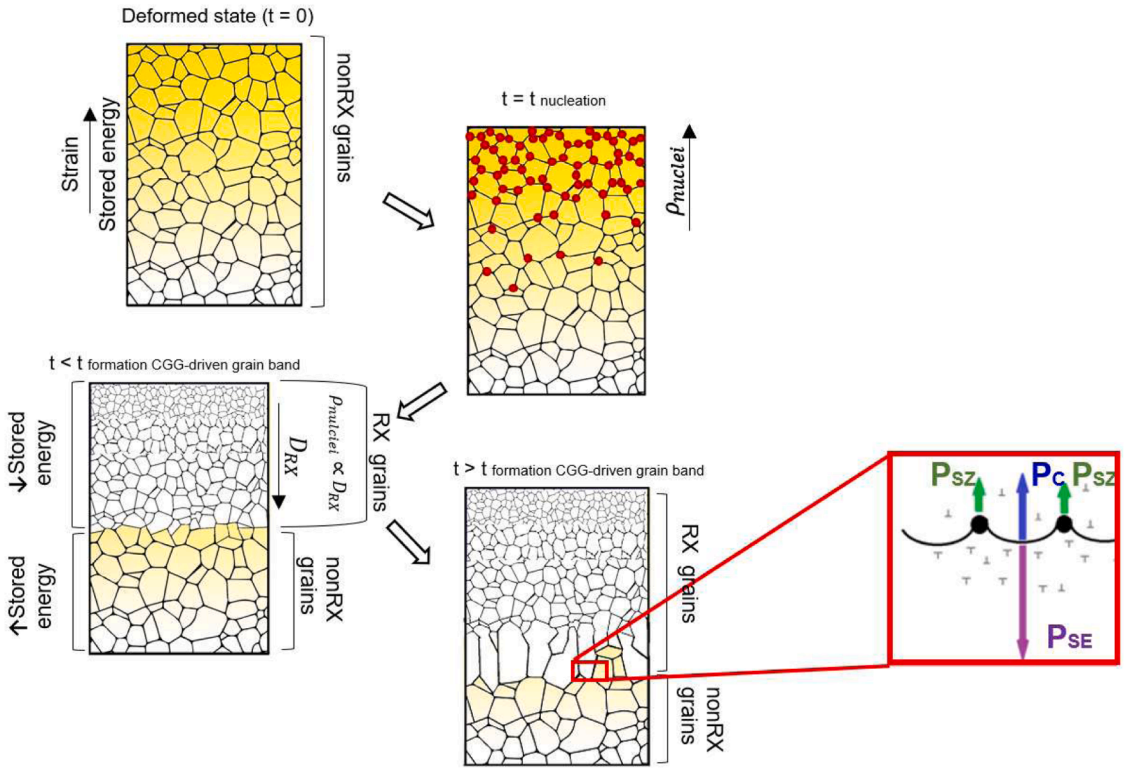

Fig. 8. Schematic illustration of the process of formation of the coarse grains band. P_{SE} refers to the pressure driven by stored energy differences, P_C is the capillarity pressure due to boundary curvature, and P_{SZ} stands for the Smith-Zener pinning pressure exerted by the second-phase particles. The nuclei are represented by red points.

area (which corresponds to the zone $\varepsilon > 0.08$, as indicated by the three upper strain-range regions in Fig. 3). Fig. 8 illustrates this behavior. Only across the grain boundaries of the recrystallized front and non-recrystallized grains there are large enough differences in stored energy such that the induced driving pressure overcomes the opposite contribution of capillarity and Smith-Zener pinning pressure [36,37] by which second-phase particles can hinder grain growth.

As Figs. 5 and 6 indicate, the expansion of the CGG-driven band does not seem to stop for all the annealing conditions analyzed. The kinetics of this band can be straightforwardly estimated, and the distance (and hence the deformed-state strain level) at which CGG stops and a stable configuration is reached can be roughly calculated. Considering that the velocity of grain boundary migration is generally described by:

$$v_{GB} = M_b \cdot P = M_b\ (P_{SE} - P_{SZ} - P_C), \tag{2}$$

where M_b $(m^4 J^{-1} s^{-1})$ is the grain boundary mobility and P is the net driving pressure. P_{SE} refers to the pressure driven by stored energy differences, P_C is the capillarity pressure due to boundary curvature and energy, and P_{SZ} stands for the Smith-Zener pinning pressure exerted by second-phase particles [38,39]. In Eq. (2), the net driving pressure for grain boundary migration in the early stages of recrystallization can be defined by the difference of P_{SE} with $P_{SZ} + P_C$ as illustrated in Fig. 8. An estimation of the different driving pressures which act on the grain boundaries that eventually lead to the formation of a coarse grains band can be done by means of 2D EBSD data [40], as detailed hereinafter.

A recrystallized grain G_i is considered, with a stored energy value of E_i. Below this grain, several non-recrystallized neighboring grains can be identified, being one of them G_j, with a mean stored energy value of E_j. The driving pressure induced by the differences in stored energy between G_i and G_j can be approximated by the following expressions:

$$P_{SE} = E_j - E_i, \tag{3}$$

and the stored energy (per grain) can be estimated following the equation [39]:

$$E = 0.5 \Delta \rho G b^2, \tag{4}$$

where ρ is the total average dislocation density (per grain), G is the shear modulus (75.8 GPa), and b is the magnitude of the Burgers vector (0.25 nm) [39,41,42].

In addition to this, note that the dislocation structure is often divided into two components: "statistically stored dislocations" (SSDs) and "geometrically necessary dislocations" (GNDs). GNDs are redundant dislocations which have a cumulative effect and therefore allow the accommodation of the lattice curvature due to a non-homogeneous plastic deformation. On the contrary, SSDs have no cumulative effects, leading to no significant rotation of the crystalline lattice and therefore have a near net-zero Burgers vector [34]. Since the EBSD technique is insensitive to SSDs and it cannot detect those dislocations with a minor disorientation level below a lower threshold, the total dislocation density will be obtained by multiplying the density of GNDs -measured by EBSD- by a constant c [15,38]. Therefore, ρ is estimated as:

$$\rho = \rho_{GND} + \rho_{SSD} = c\rho_{GND}, \tag{5}$$

Combining Eqs. (3–5), the driving pressure due to the differences in stored energy between neighboring grains can be calculated as:

$$P_{SE} = 0.5 c \Delta \rho_{GND} G b^2. \tag{6}$$

Assuming that half of all dislocations are GNDs ($c = 2$), the estimation of the pressure induced by stored energy differences at the lower boundary of the coarse grains band of Fig. 9 is $P_{SE} \approx 160\ kPa$ (after a 3 h 30 min heat treatment at 980 °C.). Note that P_{SE} value would noticeably increase if the sample had been subjected to a shorter heat treatment (higher differences in stored energy), or if a higher fraction of SSDs would have been considered.

Capillarity pressure (P_C) can be estimated by means of the following expression:

$$P_C = \frac{2\gamma}{\overline{R}_C}, \tag{7}$$

where γ is the grain boundary energy. The value of grain boundary energy is set to $\gamma = 0.6\ J/m^2$ [14]. $\overline{R}_C$ is the mean radius of the non-recrystallized grains to be consumed below the coarse grains band ($\overline{R}_C = 8\ \mu m$). Spherical grains are considered since these estimations are adapted to a 3D microstructure approximation. Thus, $P_C \approx 150\ kPa$.

Finally, the Smith-Zener pinning pressure can also be approximated, by means of the following expression [39]:

$$P_{SZ} = \frac{3\gamma f_{spp}}{d_{spp}}, \tag{8}$$

where f_{spp} is the precipitate surface fraction and d_{spp} is the precipitate

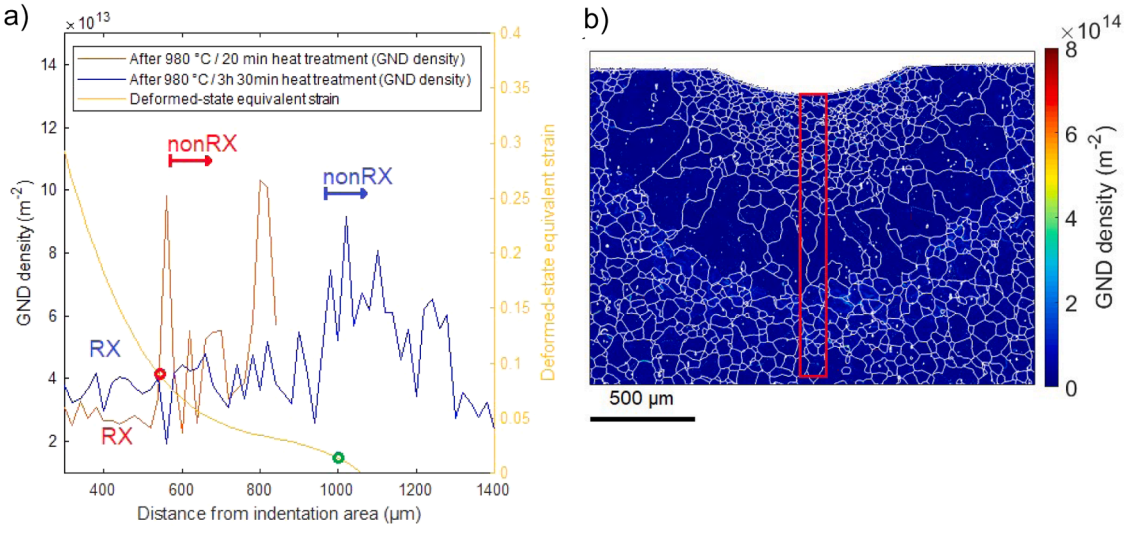

Fig. 9. (a) Deformed-state plastic equivalent strain (yellow) and the GND density profiles after a 980 °C / 20 min heat treatment (red) and after a 980 °C / 3 h 30 min heat treatment (blue). The red and green circles in the equivalent strain profile indicate, respectively, the level at which the CGG-driven band starts growing and the estimated level at which it stops growing during an annealing process at 980 °C. (b) GND density map of the 980 °C / 3 h 30 min heat-treated sample (Δcenter = 234 μm), with a rectangle in red which indicates the area used to define the GND density profile (by averaging the data along the x-axis).

average equivalent diameter. As exhibited in Fig. 10, after a 980 °C / 3 h 30 min heat treatment, there is a small increase in the density of second-phase particles with respect to the initial state previous to indentation (Fig. 1c), which could indicate that some particles precipitate during the annealing process. They can be found in the matrix and some of them are aligned in the indentation direction which coincides with the drawing direction. With $f_{spp} \approx 0.7$% and $d_{spp} \approx 1.6\ \mu m$, and therefore $P_{SZ} \approx 8\ kPa$, second-phase particles do not exert the sufficient pinning pressure to impede grain boundary migration during the heat treatment, at least with the actual volume fraction and particle size distribution.

The estimation of the driving pressures in the boundary of the coarse grains band indicates that a stable configuration might have been reached after 3 h 30 min of heat treatment at 980 °C (or between 2 h and 3 h 30 min, since there are no samples heat-treated and analyzed between these two times, as indicated in Fig. 5). The difference in the estimated values of P_{SE} and $|P_C + P_{SZ}|$ is only 2 kPa, which suggests that the coarse grains band has reached its maximum size, and the difference in stored energy between recrystallized grains and the adjacent non-recrystallized grains is not large enough to maintain grain boundary migration. As a consequence, this result leads to the definition of a critical deformed-state strain value at which recrystallized grains can grow in the presence of a strain gradient (green circle in Fig. 9a) leading to ALGs of maximum size: $\varepsilon_{crit\ ALGs} = 0.015$ according to the results from the region enclosed by a red box in Fig. 9b. The aforementioned critical strain level allows to predict the influence of CGG mechanism on static microstructural evolutions, together with the "initial" critical strain level (red circle in Fig. 9a), which indicates the critical strain level for the activation of the CGG mechanism: $\varepsilon_{crit\ CGG} = 0.084$ according to the results from the region enclosed by a red box in Fig. 4b.

3.4. Development of a nucleation law

The results discussed in this work open the perspective of developing a nucleation law for the static recrystallization process which could be implemented into full-field models such as the finite element level-set method [43] implemented in the DIGIMU® software. In this model, each grain boundary is explicitly represented and tracked during simulation using a level-set function [26,44]. The mechanism of grain boundary migration and hence grain boundary velocity can be described as the product of the competing driving pressures and a material-dependent grain boundary mobility term $M_b(T)$, as introduced in Section 3.3 (Eq. (2)). Moreover, in the DIGIMU® framework, the internal variable to control dynamic recrystallization kinetics is the dislocation density. The Yoshie-Laasraoui-Jonas phenomenological law

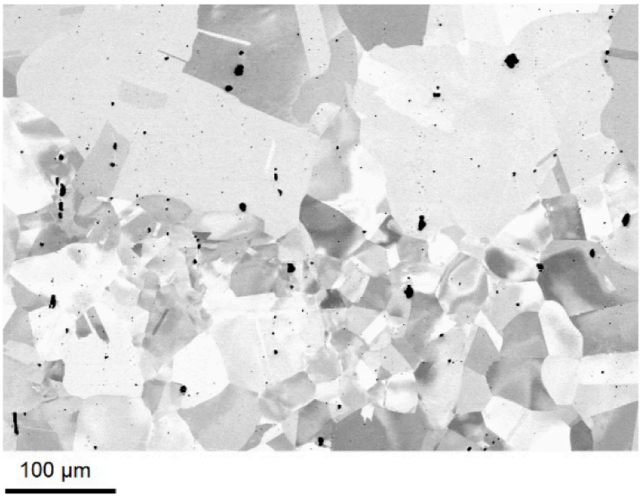

Fig. 10. BSE micrograph of the CGG-driven band and the non-RX grains below after a 980 °C / 3 h 30 min heat treatment.

is used to establish the relationship between strain and dislocation density of a grain "i" [45,46]:

$$\frac{\partial \rho_i}{\partial \varepsilon} = K_1 - K_2 \rho_i, \tag{9}$$

where K_1 and K_2 are the terms to assess the macroscopic hardening and recovery of the polycrystal, respectively.

Regarding the nucleation of recrystallized grains, considering the Bailey-Hirsch bulge mechanism [47], a critical dislocation density (ρ_{crit}) for the nucleation of recrystallized grains is set, which can be solved iteratively from the expression below in Eq. (10) [48]. This critical dislocation density is also associated to a critical recrystallized grain size (D_{crit}):

$$\rho_{crit} = \left[\frac{-\dot{\gamma}\dot{\varepsilon}\frac{K_2}{M_b \delta \tau^2}}{\ln\left(1 - \frac{K_2}{K_1}\rho_{crit}\right)} \right]^{1/2}, \tag{10}$$

$$D_{crit} = 2 \times \omega \frac{\gamma_b}{\tau(\rho_{crit} - \rho_0)}, \tag{11}$$

where δ is a strain rate dependent term for the stored energy driven grain boundary migration, ω is a numerical factor to limit mesh size effects, and $\tau(J/m)$ is the energy per unit length of dislocation line.

For all the boundaries of grains with a dislocation density above ρ_{crit}, the nucleation at grain boundaries is controlled by a nucleation rate that can be defined as [49]:

$$\dot{V}_{nucl} = K_g \Phi, \tag{12}$$

where Φ is the total length of all grain boundaries of grains with a dislocation density above $\rho_{GND\ crit}$, and K_g is a nucleation probability term.

Note that Eqs. (9–12) are only suited for a dynamic recrystallization process, with the terms K_1, K_2 and K_g dependent on the hot-deformation behavior of the material and thermomechanical conditions. An extensive experimental campaign of hot deformation tests at different thermomechanical conditions is required to obtain K_1 and K_2, and the values are fitted using the Yoshie-Laasraoui-Jonas model to approximately match the experimental data. Moreover, the parameters δ and K_g must also be refined, using direct inverse analysis with full field simulations [26]. Therefore, the modelling of static recrystallization with the current framework cannot be performed in the absence of dynamic recrystallization data, but the methodology detailed hereinafter could be used to integrate a static nucleation law in a model like DIGIMU®.

The experimental methodology presented in this work allows to determine a $\rho_{crit}(\varepsilon_{crit\ CGG},\ T)$ value (after an incubation time at a given heat treatment temperature), which corresponds to the mode in the GND density distribution from the "green" region in Fig. 3 ($\rho_{crit} \approx 1.55 \cdot 10^{14}\ m^{-2}$ at 980 °C) since the nuclei that appear further away from the indentation area (and give place to the CGG-driven recrystallized grains) are approximately located in the end (less strained area) of the "green" semi-elliptical region from Fig. 3. When the average dislocation density of a grain is above ρ_{crit}, nucleation will take place at its boundaries, where dislocation density is higher. The density of nuclei (ρ_n) is given by the number of recrystallized grains per unit area, and it can be expressed as:

$$\frac{1}{\rho_n} = K_n \frac{\overline{D}_{RX}}{Area}, \tag{13}$$

with $\rho_{GND\ grain\ "i"} \geq \rho_{crit}$ so, ρ_n is inversely correlated to the average size of the recrystallized grains for a given area (where K_n is a constant of proportionality) after nucleation and grain growth until mutual impingement. Therefore, for the three deformed-state strain semi-elliptical regions from Fig. 3, excluding the (cyan) one belonging to

the CGG-driven band, an associated $\overline{D}_{RX}$ value can be calculated in all heat treated samples (Fig. 11). In contrast to CGG-driven grains, the size of the recrystallized grains belonging to the three upper strain regions is not sensitive to the different annealing conditions. Thus a statistically relevant relationship of $\overline{D}_{RX}$ with its associated deformed-state strain value in each region, and hence with the ρ_{GND} value and distribution in that region (Fig. 3), can be established via the grain size analysis of some heat-treated specimens as depicted in Fig. 11.

Fig. 11 illustrates recrystallized grain size distributions per strain region (except in the "cyan" region of CGG-driven grains), showing that there are no significant differences in grain size distribution for different annealing times and temperatures. Once $\overline{D}_{RX}$ is calculated for each of the upper three strain regions, the following relationships can be established considering Eq. (13) and GND distribution from Fig. 3b. The threshold ρ_{GND} value is the mode of the ρ_{GND} distribution from each semi-elliptical region (Fig. 3b).

From the results displayed in Table 2, the creation of a SRX phenomenological law can be asserted as a perspective of this work. A nucleation law from indirect experimental observations (after nucleation and grain growth) as carried out in state-of-the-art nucleation models [25,50] can be proposed and would require further experimental validation. Indeed, the Yoshie-Laasraoui-Jonas law can be replaced by the resulting relationship $\rho(\varepsilon)$ from the current experiments at the temperature of 980 °C, with a ρ_{crit} value associated to the critical strain level for the activation of the CGG mechanism ($\varepsilon_{crit\ CGG}$), as defined in Section 3.2, which therefore indicates the threshold level for the nucleation and subsequent growth of recrystallized grains whose size is driven by the density of nuclei. An incubation time which increases with decreasing dislocation density could be roughly estimated from a campaign of short heat treatments, as discussed in Section 3.2. For regions associated to deformed-state strain levels above $\varepsilon_{crit\ CGG}$, a relationship between incubation time and deformed-state strain level must be estimated from the indirect calibration of the nucleation model with experimental data. In addition to this, note that the nucleation rate presented in Eq. (12) can be substituted for $\overline{D}_{RX}(\rho_{GND})$ if $\rho_{GND} \geq \rho_{crit}$ from the results in Table 2. The validation of the proposed model is left for future work.

Table 2
Density of nuclei, density of GNDs and average grain size of each of the upper three strain regions.

Deformed-state ε	Deformed-state ρ_{GND} (m^{-2})	$\overline{D}_{RX}$ (μm)	ρ_n
[0.08, 0.18]	[1.55, 2.55] $\cdot 10^{14}$	75.9	$5.6K_n$
[0.18, 0.40]	[2.55, 3.35] $\cdot 10^{14}$	46.7	$6K_n$
[0.40, 0.64]	$\rho_{GND} \geq 3.35 \cdot 10^{14}$	39.8	$7.2K_n$

4. Conclusion

The SSE levels generated by spherical indentation at room temperature were able to trigger a heterogeneous static recrystallization phenomenon in A-286 superalloy during high temperature annealing. This led to a strong grain size gradient culminating in the appearance of CGG zones. The number of active nucleation sites was proven to be highly dependent on prior strain. After nucleation, stable nuclei grow and consume the neighboring dislocation densities until mutual impingement.

Highly deformed regions give place to fine grain size distributions during solution heat treatment as a result of their high number of active nucleation sites. Conversely, low SSE regions, where nucleation is statistically less favorable, were identified as being particularly prone for CGG occurrence. The aforementioned spherical indentation experiment, and the coupling of microstructural characterization with finite element simulations, have allowed to identify two critical deformed-state strain levels in order to delimit and predict the influence of CGG mechanism on static microstructural evolutions at the temperature of 980 °C in the presence of a strain gradient (and, consequently, the formation of an abnormally large grains band and its respective size). The first one, $\varepsilon_{crit\ CGG}$, refers to the deformed-state strain level of activation of the CGG mechanism; and the second one, $\varepsilon_{crit\ ALGs}$, indicates and predicts the

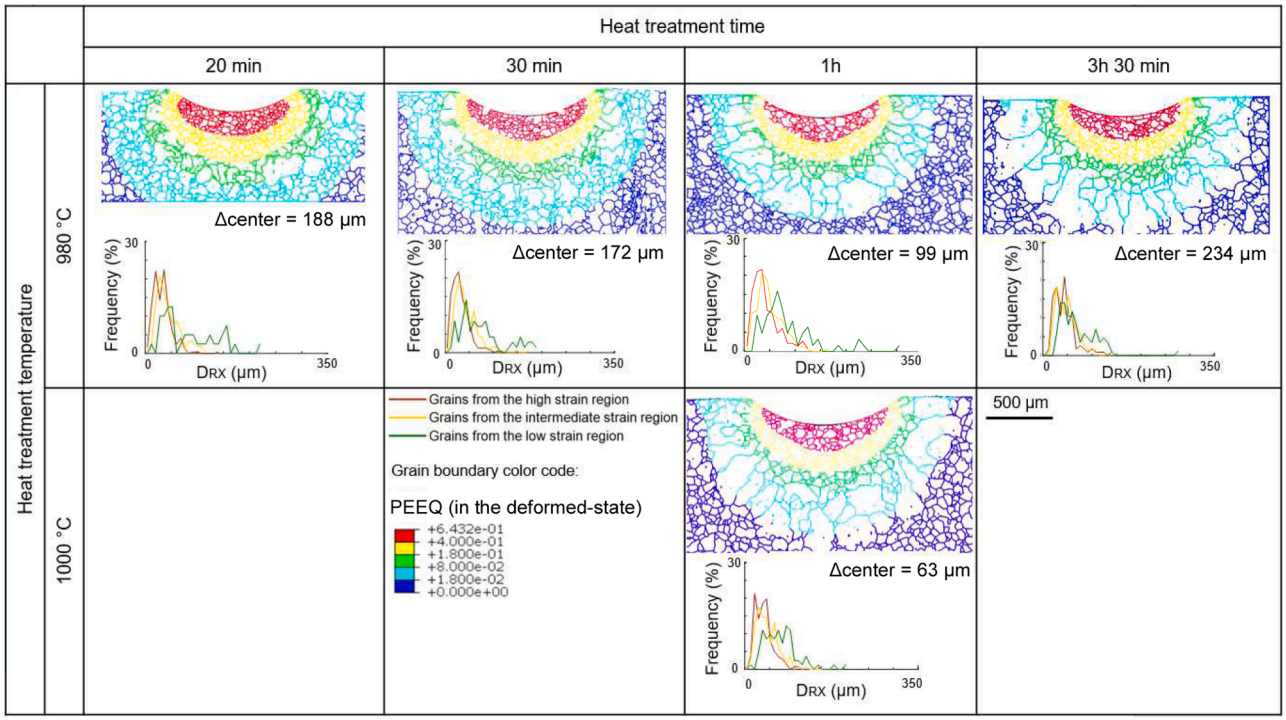

Fig. 11. Grain boundary maps of various heat-treated microstructures, including the color of their associated deformed-state strain levels identified by considering the **Δ**center value at which each map is obtained. Below, the recrystallized grain size distributions of the upper three strain regions where grain size is driven by the prior nuclei density.

deformed-state strain level up to which recrystallized grains can grow.

The spherical indentation tests successfully produced a well-controlled strain gradient to investigate the different aspects involved in the static recrystallization of strained microstructures. Short heat treatments revealed that the CGG mechanism is not triggered before 20 min of heat treatment at 980 °C. Finally, as proven for similar materials, second-phase particles, mostly titanium carbides, do not appear to be effective in hindering the migration of grain boundaries, leading to the formation of coarse grain regions. A correlation was found between the final equivalent strain field and their associated SSE levels, which can be straightforwardly estimated from the GND density value and distribution obtained by EBSD or even from hardness measurements. By means of this generic and simple approach, which could easily be reproduced in other materials, a predictive model of the static recrystallization behavior of the alloy could be calibrated from the quantitative assessment of the recrystallized grain size gradient and its dependence on stored energy, in recrystallized regions where the CGG mechanism cannot take place during the annealing process.

CRediT authorship contribution statement

A. Potenciano: Writing – original draft, Project administration, Methodology, Investigation, Conceptualization. **A. Nicolay:** Writing – review & editing, Validation, Supervision, Methodology, Investigation. **A. Da Fonseca Alvarenga:** Investigation, Conceptualization. **O. Danylova:** Validation, Supervision, Methodology. **J. Dairon:** Writing – review & editing, Validation, Supervision, Methodology. **M. Bernacki:** Writing – review & editing, Validation, Supervision, Project administration, Methodology. **B. Flipon:** Writing – review & editing, Validation, Supervision. **N. Bozzolo:** Writing – review & editing, Supervision, Project administration, Methodology, Conceptualization.

Declaration of competing interests

The authors declare that they have no known competing financial interests or personal relationships that could have appeared to influence the work reported in this paper.

Acknowledgements

This study was carried out with Aperam funding and support, within the framework of the DIGIMU consortium, handled by MINES Paris and Armines.

References

[1] A.P. Mouritz, Introduction to Aerospace Materials, RMIT University, Melbourne, 2012, https://doi.org/10.2514/4.869198, 1st.
[2] M. Alizadeh-Sh, S.P.H. Marashi, E. Ranjbarnodeh, R. Shoja-Razavi, Laser cladding of Inconel 718 powder on a non-weldable substrate: clad bead geometry-solidification cracking relationship, J. Manuf. Process. 56 (2020) 54–62, https://doi.org/10.1016/j.jmapro.2020.04.045.
[3] J. Miao, T.M. Pollock, J.W. Jones, Crystallographic fatigue crack initiation in nickel-based superalloy René 88DT at elevated temperature, Acta Mater. 57 (2009) 5964–5974, https://doi.org/10.1016/j.actamat.2009.08.022.
[4] B. Flageolet, O. Yousfi, Y. Dahan, P. Villechaise, J. Comier, Characterization of microstructures containing abnormal grain growth zones in Alloy 718, in: Proceedings of the 7th International Symposium on Superalloy 718 and Derivatives, 2010, pp. 595–606, https://doi.org/10.1002/9781118495223.ch46.
[5] T.P. Gabb, P.T. Kantzos, J. Telesman, J. Gayda, C.K. Sudbrack, B. Palsa, Fatigue resistance of the grain size transition zone in a dual microstructure superalloy disk, Int. J. Fatigue 33 (2011) 414–426, https://doi.org/10.1016/j.ijfatigue.2010.09.022.
[6] X. Huang, J. Li, B.S. Amirkhiz, P. Liu, Effect of water density on the oxidation behavior of alloy A-286 at 625 °C - A TEM study, J. Nucl. Mater. 467 (2015) 758–769, https://doi.org/10.1016/j.jnucmat.2015.10.023.
[7] O. Takakuwa, Y. Ogawa, J. Yamabe, H. Matsunaga, Hydrogen-induced ductility loss of precipitation-strengthened Fe-Ni-Cr based superalloy, Mater. Sci. Eng. A 739 (2019) 335–342, https://doi.org/10.1016/j.msea.2018.10.040.
[8] Z. Guo, H. Liang, M. Zhao, L. Rong, Effect of boron addition on hydrogen embrittlement sensitivity in Fe–Ni based alloys, Mater. Sci. Eng. A 527 (24–25) (2010) 6620–6625, https://doi.org/10.1016/j.msea.2010.06.07.
[9] L. Wei, H. Zhao, Y. Sun, Y. Zhang, B. Zhao, Z. Liu, J. Liang, Z. Yang, Microstructure evolution and stress rupture properties of A286 superalloy in the 600 °C to 750 °C temperature range, Mater. Res. Exp. 8 (2) (2021) 026521, https://doi.org/10.1088/2053-1591/abe6d4.
[10] J.D. Kazimierz, Analysis of the precipitation and growth process of the intermetallic phases in an Fe-Ni superalloy, Superalloys. Chapter 6, Intech Open, Poland, 2015, https://doi.org/10.5772/61159.
[11] M.A. Charpagne, J.M. Franchet, N. Bozzolo, Overgrown grains appearing during sub-solvus heat treatment in a polycrystalline γ-γ' Nickel-based superalloy, Mater. Des. 144 (2018) 353–360, https://doi.org/10.1016/j.matdes.2018.02.048.
[12] V.M. Miller, A.E. Johnson, C.J. Torbet, T.M. Pollock, Recrystallization and the development of abnormally large grains after small strain deformation in a polycrystalline nickel-based superalloy, Metallur. Mater. Trans. A 47 (2016) 1566–1574, https://doi.org/10.1007/s11661-016-3329-6.
[13] X. Wang, Z. Huang, B. Cai, N. Zhou, O. Magsysyuk, Y. Gao, S. Srivatsa, L. Tan, L. Jiang, Formation mechanism of abnormally large grains in a polycrystalline Nickel-based superalloy during heat treatment processing, Acta Mater. 168 (2019) 287–298, https://doi.org/10.1016/j.actamat.2019.02.012.
[14] A. Agnoli, M. Bernacki, R. Logé, J.-M. Franchet, J. Laigo, N. Bozzolo, Selective growth of low stored energy grains during δ sub-solvus annealing in the Inconel 718 nickel-based superalloy, Metallur. Mater. Trans. A 46 (2015) 4405–4421, https://doi.org/10.1007/s11661-015-3035-9.
[15] A. Agnoli, M. Bernacki, R. Loge, J.-M. Franchet, J. Laigo, N. Bozzolo, Understanding and modeling of grain boundary pinning in Inconel 718, in: Superalloys 2012, 12th Int. Symp. Superalloys Proceedings, 2012, pp. 73–82, https://doi.org/10.1002/9781118516430.ch8.
[16] N. Bozzolo, A. Agnoli, N. Souaï, M. Bernacki, R.E. Logé, Strain induced abnormal grain growth in nickel base superalloys, Mater. Sci. Forum 753 (2013) 321–324, https://doi.org/10.4028/www.scientific.net/MSF.753.321.
[17] C. Aoki, T. Ueno, T. Ohno, K. Oikawa, Influence of hot-working conditions on grain growth of superalloy 718, J. Mater. Proces. Tech. 267 (2019) 26–33, https://doi.org/10.1016/j.jmatprotec.2018.12.002.
[18] S. Vernier, MINES ParisTech-PSL, PhD thesis, 2018.
[19] P.A. Manohar, M. Ferry, T. Chandra, Five decades of the Zener Equation, ISIJ Int. 38 (1998) 913–924, https://doi.org/10.2355/isijinternational.38.913.
[20] M. Avrami, Kinetics of phase change. I general theory, J. Chem. Phys. 7 (1939) 1103–1112, https://doi.org/10.1063/1.1750380.
[21] M. Avrami, Kinetics of phase change. II transformation–time relations for random distribution of nuclei, J. Chem. Phys. 8 (1940) 212–224, https://doi.org/10.1063/1.1750631.
[22] M. Avrami, Granulation, phase change, and microstructure kinetics of phase change. III, J. Chem. Phys. 9 (1941) 177–184, https://doi.org/10.1063/1.1750872.
[23] M. Bernacki, Kinetic equations and level-set approach for simulating solid-state microstructure evolutions at the mesoscopic scale: state of the art, limitations, and prospects, Prog. Mater. Sci. 101224 (2024), https://doi.org/10.1016/j.pmatsci.2023.101224.
[24] H. Hallberg, A modified level set approach to 2D modeling of dynamic recrystallization, Modell. Simul. Mater. Sci. Eng. 21 (2013) 085012, https://doi.org/10.1088/0965-0393/21/8/085012.
[25] L. Maire, B. Scholtes, C. Moussa, N. Bozzolo, D.P. Muñoz, A. Settefrati, M. Bernacki, Modeling of dynamic and post-dynamic recrystallization by coupling a full field approach to phenomenological laws, Mater. Des. 133 (2017) 498–519, https://doi.org/10.1016/j.matdes.2017.08.015.
[26] B. Flipon, N. Bozzolo, Marc Bernacki, A simplified intragranular description of dislocation density heterogeneities to improve dynamically recrystallized grain size predictions, Materialia 26 (2022) 101585, https://doi.org/10.1016/j.mtla.2022.101585.
[27] A. Nicolay, J.M. Franchet, J. Cormier, H. Mansour, M. de Graef, A. Seret, N. Bozzolo, Discrimination of dynamically and post-dynamically recrystallized grains based on EBSD data: application to Inconel 718, J. Microsc. 00 (2018) 1–13, https://doi.org/10.1111/jmi.12769.
[28] F. Bachmann, R. Hielscher, H. Schaeben, Grain detection from 2D and 3D EBSD data—Specification of the MTEX algorithm, Ultramicroscopy 111 (2011) 1720–1733, https://doi.org/10.1016/j.ultramic.2011.08.002.
[29] R. Bergmann, R.H. Chan, R. Hielscher, J. Persch, G. Steidl, Restoration of manifold-valued images by half-quadratic minimization, Inv. Probl. Imag. 10 (2016) 281–304, https://doi.org/10.3934/ipi.2016001.
[30] & P. Lehto, Remes, EBSD characterisation of grain size distribution and grain sub-structures for ferritic steel weld metals, Weld. World 66 (2) (2022) 363–377, https://doi.org/10.1007/s40194-021-01225-w.
[31] ABAQUS/Standard User's Manual for Version 6.5.1, Hibbitt, Karlsson and Sorensen Inc., 2004.
[32] J.F. Nye, Some geometrical relations in dislocated crystals, Acta metallurg. 1 (2) (1953) 153–162, https://doi.org/10.1016/0001-6160(53)90054-6.
[33] W. Pantleon, Resolving the geometrically necessary dislocation content by conventional electron backscattering diffraction, Scr. Mater. 58 (11) (2008) 994–997, https://doi.org/10.1016/j.scriptamat.2008.01.050.
[34] L.E. Samuels, T.O. Mulhearn, An experimental investigation of the deformed zone associated with indentation hardness impressions, J. Mech. Phys. Solids 5 (2) (1954) 125–134, https://doi.org/10.1016/0022-5096(57)90056-X.
[35] P.S. Phani, W.C. Oliver, A critical assessment of the effect of indentation spacing on the measurement of hardness and modulus using instrumented indentation testing, Mater. Des. 164 (1949) 107563, https://doi.org/10.1016/j.matdes.2018.107563.

[36] C. Smith, Introduction to grains, phases, and interfaces—An interpretation of microstructure, Trans. AIME 175 (1948) 15–51, https://doi.org/10.1007/s11663-010-9364-6.
[37] C. Zener, Theory of growth of spherical precipitates from solid solution, J. Appl. Phys. 20 (1949) 950–953, https://doi.org/10.1063/1.1698258.
[38] A. Seret, C. Moussa, M. Bernacki, J. Signorelli, N. Bozzolo, Estimation of GND density from filtered EBSD data by automatic local linear calibration of smoothing splines, J. Appl. Crystallogr. 52 (2019) 548–563, https://doi.org/10.1107/S1600576719004035.
[39] A. Rollett, G.S. Rohrer, J. Humphreys. Recrystallization and Related Annealing Phenomena, 3rd Edition, Newnes, Oxford, UK, 2017.
[40] S. Ouhiba, A. Nicolay, L. Boissonnet, M. Bernacki, N. Bozzolo, Formation of coarse recrystallized grains in 6016 aluminum alloy during holding after hot deformation, Metallur. Mater. Trans. A 53 (7) (2022) 2402–2425, https://doi.org/10.1007/s11661-022-06672-8.
[41] H. Ledbetter, W. Weston, E. Naimon, Low-temperature elastic properties of four austenitic stainless steels, J. Appl. Phys. 46 (9) (1975) 3855–3860, https://doi.org/10.1063/1.322182.
[42] M. Savoie, C. Esnouf, L. Fournier, D. Delafosse, Influence of ageing heat treatment on alloy a-286 microstructure and stress corrosion cracking behaviour in pwr primary water, J. Nucl. Mater. 360 (3) (2007) 222–230, https://doi.org/10.1016/j.jnucmat.2006.10.003.
[43] M. Bernacki, Kinetic equations and level-set approach for simulating solid-state microstructure evolutions at the mesoscopic scale: state of the art, limitations, and prospects, Prog. Mater. Sci. 142 (2024) 101224, https://doi.org/10.1016/j.pmatsci.2023.101224.
[44] B. Murgas, B. Flipon, N. Bozzolo, M. Bernacki, Level-set modeling of grain growth in 316L stainless steel under different assumptions regarding grain boundary properties, Materials 15 (7) (2022), https://doi.org/10.3390/ma15072434.
[45] A. Yoshie, H. Morikawa, Y. Onoe, K. Itoh, Formulation of static recrystallization of austenite in hot rolling process of steel plate, Trans. ISIJ 27 (1987) 425–431, https://doi.org/10.2355/isijinternational1966.27.425.
[46] A. Laasraoui, J. Jonas, Prediction of steel flow stresses at high temperatures and strain rates, Metall. Trans. A 22A (1991) 1545–1558, https://doi.org/10.1007/BF02667368.
[47] J. Bailey, P. Hirsch, N. Mott, The recrystallization process in some polycrystalline metals, Proc. R. Soc. 267 (1962), https://doi.org/10.1098/rspa.1962.0080. London.
[48] W. Roberts, B. Ahlblom, A nucleation criterion for dynamic recrystallization during hot working, Acta Metall. 26 (1978) 801–813, https://doi.org/10.1016/0001-6160(78)90030-5.
[49] P. Peczak, M Luton, The effect of nucleation models on dynamic recrystallization I. Homogeneous stored energy distribution, Phil. Mag. B 68 (1993) 115–144, https://doi.org/10.1080/13642819308215285.
[50] B. Scholtes, R. Boulais-Sinou, A. Settefrati, D.P. Muñoz, I. Poitrault, A. Montouchet, N. Bozzolo, M. Bernacki, 3D level set modeling of static recrystallization considering stored energy fields, Comput. Mater. Sci. 122 (2016) 57–71, https://doi.org/10.1016/j.commatsci.2016.04.045.